Advanced Materials Interfaces

ADVANCED MATERIALS INTERFACES Open Access

www.advmatinterfaces.de

RESEARCH ARTICLE OPEN ACCESS

Centrifugation Theory Revisited: Understanding and Modeling the Centrifugation of 2D Nanosheets

Stuart Goldie[1] | Steffen Ott[2] | Anthony Dawson[3] | Tamara Starke[2] | Cian Gabbett[3] | Victor Vega-Mayoral[4] | Kevin Synnatschke[2,3,5] | Marilia Horn[1,6] | Jonathan N. Coleman[3] | Claudia Backes[1,2]

[1]Physical Chemistry of Nanomaterials and CINSaT, Kassel University, Kassel, Germany | [2]Applied Physical Chemistry, Heidelberg University, Heidelberg, Germany | [3]School of Physics and CRANN, Trinity College, Dublin 2, Ireland | [4]Instituto Madrileño De Estudios Avanzados En Nanociencia (IMDEA), Madrid, Spain | [5]Chair For Molecular Functional Materials, Dresden University of Technology, Dresden, Germany | [6]Institute for Molecular Microbiology and Biotechnology (IMMB), University of Münster, Münster, Germany

Correspondence: Jonathan N. Coleman (colemaj@tcd.ie) | Claudia Backes (backes@uni-kassel.de)

Received: 5 August 2025 | **Revised:** 10 November 2025 | **Accepted:** 10 November 2025

Keywords: 2D materials | centrifugation | solution Processing | size control | theoretical framework

ABSTRACT

Size selection of liquid-dispersed 2D nanomaterials is a prerequisite for size-dependent studies in earlier-stage research and for their targeted application in commercial settings. Centrifugation is the most widespread method for reliably sorting suspensions of polydisperse 2D nanosheets according to size. However, whilst centrifugation is effective, no a priori models are available to predict the outcome of centrifugation, making time-consuming iterative experiments necessary. Here, we present a simple model for the behavior of 2D nanosheets during centrifugation and benchmark its predictions against experiments. This model uses simple expressions, specific to 2D particles, for the hydrodynamic radius, effective density, and viscous resistance to generate the equation of motion of individual nanosheet during centrifugation. Critically, the equation of motion is then used to predict nanosheet size distributions within centrifugation products. This in turn leads to equations for easily measurable properties such as mean and maximum nanosheet sizes obtained during centrifugation-based fractionation. Comparison with experimental data demonstrates the robustness of this model for a range of 2D materials and solvent systems, and its ability to describe quite subtle effects. These results will enable more tailored size selection of nanosheets for specific applications and offer new mechanistic insights to optimize exfoliation conditions.

1 | Introduction

Liquid processable formulations of 2D materials hold great promise to capitalize on the remarkable properties offered by these exciting nanomaterials. By employing top-down exfoliation in liquids, a vast array of crystalline and powdered materials can be converted into nanosheets in colloidally stable liquid dispersions suitable for printing [1, 2], self-assembly [3], chemical functionalization [4, 5], and incorporation into polymer matrices [6]. Today, such methods offer variety in the size and shape of nanosheets produced: sonication-assisted liquid phase exfoliation (LPE) produces small, highly fragmented sheets [7]; shear-dominated LPE generally produce slightly larger and thicker sheets [8]; electrochemical methods can produce laterally larger and thinner sheets [9], and chemical intercalation generally produces doped or chemically-modified nanosheets of similarly large aspect ratios [10]. The wide range of nanosheet shapes and sizes that can be produced is promising because it allows production methods to be matched with targeted applications. However, this breadth of nanosheet sizes that can be prepared, even within a single sample, can also pose many challenges in terms of accurate determination of lateral size and thickness

distributions on the one hand and to the purification and isolation of the desired nanosheet size on the other.

All top-down exfoliation methods produce a poly-disperse mixture of nanosheet lengths and thicknesses, which have a correspondingly wide range of properties due to the size dependence of these materials [11]. To fully exploit such dispersions, a reliable method for targeting specific nanosheets sizes for use in specific applications is required. To-date centrifugation has remained the primary method of size selection for liquid dispersions of nanosheets because it is simple to implement, and works for all materials, regardless of their physical or chemical properties. Although simple preparative centrifuge experiments have long been known to separate larger nanosheets in the sediment from smaller nanosheets remaining in the supernatant, it has not been possible to predict the nanosheet sizes in each fraction without prior experimentation.

It must be acknowledged that colloidal dispersions of 2D particles have been investigated for many decades, and numerous particle sizing methods have been introduced, including measuring translation and rotational diffusion, area and volume projection, and sedimentation [12]. These have been applied to many materials, including laponite, talc, kaolinite, illite, and montmorillonite [13–15]. However, also in these cases, it has not been possible to predict and control the purification of different particle sizes.

To more precisely separate different nanosheet sizes, density gradient ultracentrifugation has been used on 1D carbon nanotubes and 2D nanosheets such as graphene and transition metal dichalcogenides (TMDCs) [16–19]. In this process, the nanomaterial is dispersed in a density gradient medium and the experiment run for a long time until all nanosheets reach their neutrally buoyant positions. Since all particles have a bound hydration layer with a constant thickness, their effective density varies with particle volume and different-sized particles can be extracted from different points in the density gradient. For 2D nanosheets, this allows for a sorting by thickness. It can provide exquisite control over nanosheet thickness but requires very long timescales and expensive equipment to produce relatively dilute samples. For example, for monolayer MoS_2, a yield of 2 μg per separation has been reported [18]. Furthermore, the addition of density gradient media is required, often solutions of sugars, which need to be removed prior to further processing.

An alternative method for size separation using commonly available benchtop centrifuges is liquid cascade centrifugation (LCC) [20]. This widely used method [21–28] has been discussed in recent reviews for graphene and metal chalcogenides, and reported for a range of materials including MXenes [21, 29]. By sequentially increasing the centrifuge speed (or time) over multiple centrifugation steps and extracting the sediment from each step, a series of samples are obtained. These contain decreasing nanosheet size with each centrifugation run. Microscopy and spectroscopy studies of these samples clearly showed well-separated size distributions. However, different suspensions, for example, with nanosheets of dissimilar density or solvents of differing viscosity, respond quantitatively differently to the same processing conditions. If these differences are not accounted for, it is problematic to benchmark new materials or production methods against established procedures. For example, particle sedimentation in viscous solvents or media is slower [30], which can lead to an overestimation of dispersed concentration after removal of unexfoliated material and hence yield and production rate.

To allow more reliable comparisons between solvent systems, density and viscosity have been used to normalize the relative centrifugal force applied to nanosheets [21, 31]. A geometric mean sheet size approximation has also been applied to LCC to estimate the sheet size in each fraction [32]. However, no complete consideration of surfactant coating or the various geometric effects specific to the dimensionality of 2D nanosheet systems has been reported so that it is not possible to accurately predict the outcome of a centrifugation run, never mind size selection through a cascade of iterative runs.

Although analytical ultracentrifugation has been used to gather more information about the sedimentation of particles of various shapes, it has some limitations. For 1D nanoparticles, such as carbon nanotubes, analytical ultracentrifuge experiments have proved successful at characterizing the effect of the surfactant on the buoyant density of the colloid. Specifically, the surfactant packing density and thickness around single-walled carbon nanotubes in aqueous solution has been investigated by resolving the nanotube concentration as a function of position and time during centrifugation, and fitting this to a theoretical model describing nanotube sedimentation and diffusion [33, 34]. However, the effect of the dimensionality of the particles on viscous friction was not accurately modeled. When applied to polydisperse samples of 2D materials, analytical ultracentrifugation has proved capable of determining the lateral sheet size distribution of monolayer graphene oxide [35]. Furthermore, a mathematical framework was developed to describe particle separation of multi-dimensional lognormal distributions [36], which lays the foundation to use analytical ultracentrifugation to determine the particle size distribution in terms of both thickness and length in a 2D nanosheet dispersion in the future. Nevertheless, while enormously powerful, such experiments require specialized ultracentrifuges capable of spatially resolving (optical) spectra from revolving centrifuge cells, that are not routinely available in research labs. Further, the determination of particle size distributions requires an accurate description of the shape-dependent sedimentation and diffusion behavior which is currently lacking.

In the context of preparatory centrifuge experiments performed in the lab, and the development of larger-scale production of 2D materials, knowledge of the sedimentation dynamics that can be easily calculated for new and existing materials would allow a more targeted approach to size selection. Especially if such predictions can be extended from the motion of an individual sheet to the change of the distribution of nanosheets within a dispersion in response to centrifugation. An improved theoretical framework that explicitly accounts for the dimensionality of 2D nanosheets would also aid size dependency studies and exfoliation comparisons for new methods and solvent systems. For example, such a framework would complement analytical ultracentrifugation, establishing it as an efficient tool to determine nanosheet size and thickness distributions in a dispersion without the need for microscopy statistics.

To solve this problem, we introduce a simple model incorporating hydrodynamic radius, effective density, and viscosity, specific to nanosheets. This allows us to derive a sedimentation coefficient accounting for the particles' shape and surfactant coating. A comparison of the predicted sedimentation behavior to experimental data collected from 2D nanosheets separated by band sedimentation in a swinging bucket rotor proves the accuracy of the sedimentation coefficient. With this accurate description of the sedimentation velocity, we also show that it is possible to calculate the relative population changes in polydisperse mixtures and make predictions of average nanosheet size following a centrifugation cascade in the commonly used fixed-angle rotors. Experimental data of >10 cascade centrifugation sets on a range of materials and in different solvent systems is well described by the model confirming the broader applicability.

2 | Results and Discussion

2.1 | Generating the Equation of Motion for Nanosheets in a Centrifugal Field

In a centrifugal field, mobile particles will experience a centrifugal force, viscous resistance from their motion through the fluid and the effects of buoyancy from the weight of solvent displaced. By assuming rapid acceleration to terminal velocity, Svedberg resolved these forces to express the sedimentation velocity, v, as [30]:

$$\frac{dr}{dt} = v = \frac{r\omega^2 m}{f}\left(\frac{\rho_{eff} - \rho_l}{\rho_{eff}}\right) \tag{1}$$

here, m is the particle mass, r is the instantaneous distance of the particle from the center of rotation and ω is angular velocity, such that $F_c = mr\omega^2$ is the centrifugal force. In addition, f is the friction coefficient, which relates the viscous frictional force to particle velocity, $F_f = fv$ [37]. The final term is the buoyancy correction factor where ρ_{eff} is the effective density of the particle and ρ_l is that of the liquid. The effective density should account for any tightly bound surfactant on the particle surface, slightly reducing the density of the object compared to the particle core.

Separating out the experimental conditions of centrifuge radius and speed, a sedimentation coefficient (S) can be defined that contains all the contributions from the material density, shape, and size effects on its sedimentation velocity.

$$v = Sr\omega^2 \tag{2a}$$

Such that

$$S = \frac{m}{f}\left(\frac{\rho_{eff} - \rho_l}{\rho_{eff}}\right) \tag{2b}$$

We note that Equations (1) and (2a,b) are completely general and apply to all particles. Specifying these equations for a specific geometry requires modification of the parameters included in S. While sedimentation coefficients are well-defined for spheres, they are much harder to quantify for other geometries, especially when the particle is coated with a surfactant. To find S for a 2D nanosheet, Equation (2b) must be corrected for the effect of surfactant on ρ_{eff}. In addition, f must be modified considering the effect of geometry on both the hydrodynamic radius of the nanosheet and the extra viscous resistance felt by non-spherical objects (see below and Supporting Information). Although various papers have considered one or even two of these factors for quasi-2D particles [17, 19, 35, 36], none have correctly treated all three factors and, in particular, none have properly treated the extra non-spherical drag.

Here, we consider all three effects to fully quantify sedimentation of 2D nanosheets. Full details of this derivation are provided in Section S2.1, but the key steps and assumptions are summarized here. We note that, as shown in Section S2.8, considering the Peclet number for nanosheets sinking in a centrifuge allows us to rule out the need to include diffusion effects in this system (except at unrealistically small values of ω).

To specify S for 2D nanosheets, we first address the effective mass (mass times buoyancy correction factor). We use a simple geometric model illustrated in Figure 1A, approximating the platelets as quasi-2D prisms of area A and thickness, h, coated top and bottom with a surfactant layer of thickness d. Then, the effective mass of the surfactant-coated nanosheet is:

$$m\left(\frac{\rho_{eff} - \rho_l}{\rho_{eff}}\right) = \left(h\left(\rho_{NS} - \rho_l\right) + 2d\left(\rho_S - \rho_l\right)\right)A \tag{3}$$

where ρ_{NS}, ρ_l and ρ_S refer to densities of nanosheet, solvent and surfactant layer respectively (see Supporting Information).

Next, we specify the effect of friction for 2D nanosheets. To do this, we note that for non-spherical particles, the frictional coefficient is given by a simple modification of Stokes law: $f = 6\pi\eta c f_0$ [37, 38]. Here c is the hydrodynamic radius of the nanosheet, f_0 is a geometric correction factor and η is the viscosity of the fluid. We approximate c as the radius of a sphere of equal volume to the surfactant-coated nanosheet. In addition, we approximate f_0 by taking the expression given in refs. [37–39] which describes the correction factor for an oblate spheroid and taking its limit where the spheroid lateral size far exceeds its thickness (see Section S2.1). Combining these approximations gives an equation for the friction coefficient of a surfactant-coated nanosheet:

$$f = 6\pi\eta\left(\frac{3A\left(h+2d\right)}{4\pi}\right)^{1/3}\frac{2}{\pi}\left(\frac{\sqrt{A}}{h+2d}\right)^{1/3} = 12\eta\left(\frac{3}{4\pi}\right)^{1/3}A^{1/2} \tag{4}$$

The advantage of using the spheroid model for f is that we obtain a relatively simple equation in contrast to the truncated approximations required by other models using discontinuous shapes like cylinders and disks [40].

Oblate spheroids have previously been used to describe the sedimentation of colloidal platelets, modeled as hard disks by van der Kooij [41]. However, they omit an aspect ratio dependency on friction, as found in other models, to account for the relaxation at terminal velocity [12]. Additionally, we integrate this model into a geometric description of 2D nanosheets more relevant to common microscopy measurements.

Combining these contributions produces an expression for the sedimentation velocity of a 2D platelet, radially outwards away

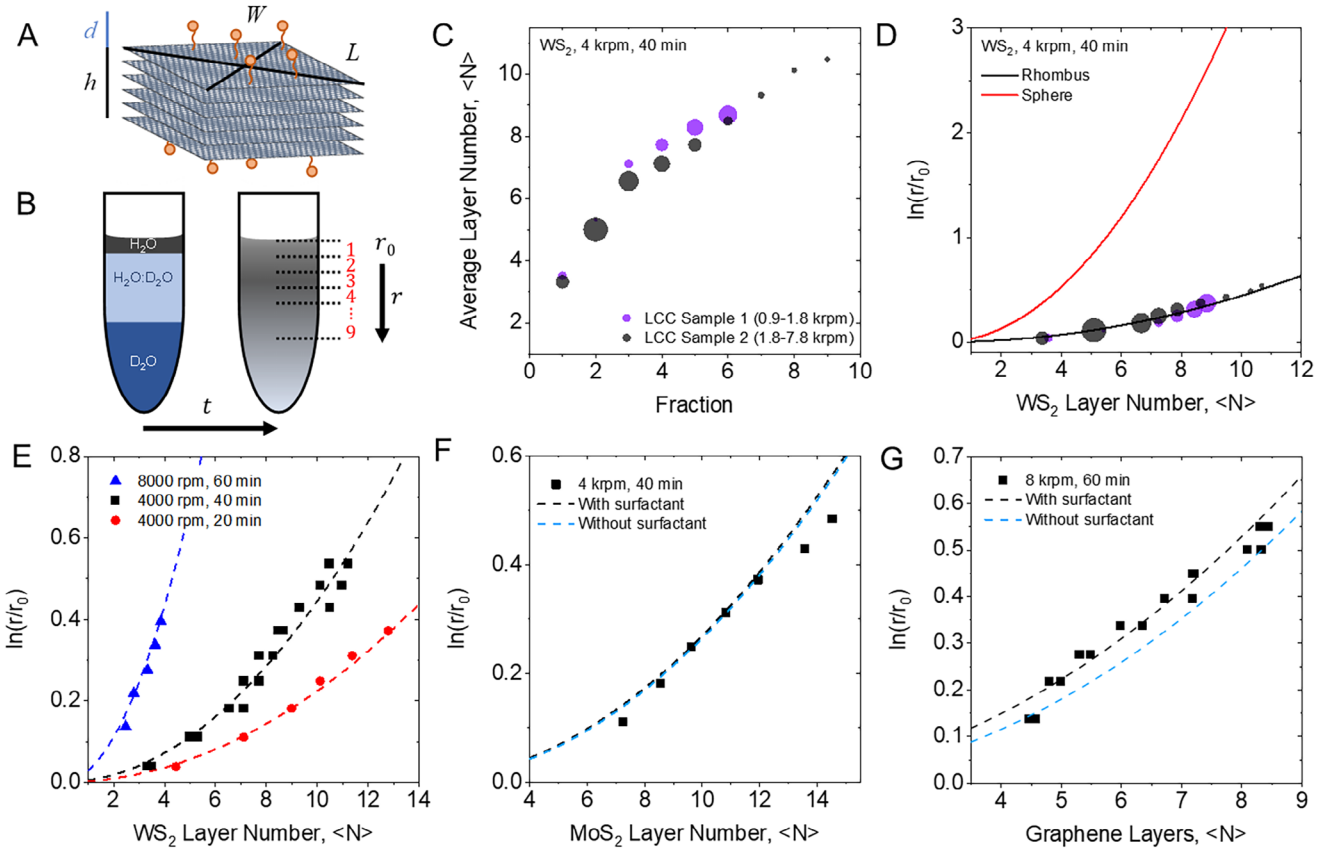

FIGURE 1 | Band sedimentation (swinging bucket rotor). A) Schematic of the rhombohedral nanosheet with surfactant coating. B) Schematic of the band sedimentation experiment indicating the withdrawal of fractions from top to bottom after centrifugation. C) Plot of average layer number (of WS_2) of the fractions extracted at different positions in the centrifuge tube after centrifugation at 4 krpm for 40 min. The differently colored datasets were obtained from WS_2 dispersions with different initial size/thickness distribution and the data point diameter is proportional to concentration. D) Same data as in (C) presented as plot of $\ln(r/r_0)$ as function of WS_2 layer number. The solid lines represent the expectation from theory with spherical platelets (red) and rhombus (black). E–G) Plot of $\ln/r/r_0$ as function of nanosheet layer number. Dashed lines show the expectation from theory. E) WS_2 dispersions centrifuged for different times. F) MoS_2. G) Graphene.

from the axis of rotation:

$$\frac{dr}{dt} = \left(\frac{(h\Delta\rho_{NS} + 2d\Delta\rho_S) A^{1/2}}{12\eta(3/4\pi)^{1/3}} \right) r\omega^2 = S(h, A)\, r\omega^2 \qquad (5)$$

where $\Delta\rho_{NS}$ is the density difference of nanosheet and liquid medium and $\Delta\rho_S$ the density difference of surfactant and liquid medium. If the distance from center of rotation to a platelet is known at $t = 0$, labeled r_0, solving this differential equation allows us to calculate the position of the platelet after time t:

$$r = r_0 e^{S(h,A)\omega^2 t} \qquad (6)$$

where all dependency on sheet size, shape, and surfactant coating (if applicable) is included within the sedimentation coefficient S. For comparison, the sedimentation coefficient of spherical particles with a surfactant coating is given in Equation S2. We note that some experimental factors included within S, specifically the density and viscosity of the liquid medium, vary with temperature as well as composition. Rotation speed and time are explicitly included in the exponent, and r and r_0 are the final and initial radial positions from the center of rotation which depend on the centrifuge rotor used.

2.2 | Experimental Confirmation of the Equation of Motion

To experimentally confirm the validity of this model we used band (or rate zonal) sedimentation of WS_2, MoS_2 and graphene nanosheets prepared by LPE in aqueous surfactant; specific details in Methods, Section S3. Band sedimentation is useful as it can be employed to cleanly separate materials with different sedimentation coefficients [42–45]. In this technique, a concentrated dispersion of mixed particles is floated above pure solvent, in this case a water and heavy-water mixture as illustrated in Figure 1B, and the sample centrifuged at a certain speed and time so that the nanomaterial becomes spread throughout the vial after the run. Here, heavy-water establishes a subtle density gradient to stabilize the bands [46] (and facilitate the initial layering), but otherwise plays no role in the separation process. Such experiments are completed with swinging-bucket rotors so particle movement is parallel with the centrifugal field, down the tube. As such, the experiment allows the validation of Equation (6), by determining the nanosheet sizes at different distances from the rotation axis (along with all other parameters encoded in S). Density and viscosity values of the liquid medium in the centrifuge tube were found from the average composition, discussed in Section S4.1.

The bands from which the technique gets its name are formed when different sized particles sediment at different rates. If the sizes are sufficiently different, horizonal "bands" are observed down the tube, and from the distance these bands travel, sedimentation coefficients can be calculated. Typical dispersions of 2D materials do not have such discrete sizes for distinct bands to form leading to a broad spread in final nanosheet positions. However, fractions can be removed from specific radii (r) down the tube and the nanosheet average size or size distribution measured.

Using established metrics from UV/VIS extinction spectroscopy [47, 48], we determined the average nanosheet thickness and concentration in each fraction (full spectra are shown in Section S4.2). This is visualized for WS_2 samples in Figure 1C, where we note the steady trend of increasing sheet layer number further down the tube. Data from two different samples are shown, each subjected to different pre-processing to select different size distributions before the band sedimentation. Using different size distributions of sheets clearly has no bearing on the sedimentation dynamics, since the average thickness in each fraction is consistent between samples. But the concentrations measured, shown by the area of the data points, reflects the different make-up of the two pre-size selected samples.

For band sedimentation, the distance of the top layer from the rotation axis is r_0 and the distance at the midpoint of each fraction is r. This allows us to plot this data to compare experiment with the theoretical sedimentation coefficient derived above. However, thus far we have considered 2D materials with an area and thickness, which results in a multidimensional equation. This can be simplified using average aspect ratios that are known for common materials prepared by LPE [49]. This is because thermodynamic studies of the exfoliation process have shown that the sheet scission and exfoliation events follow principles of equipartition [50]: as energy is applied to break bonds, the proportion of inter- and intra-layer bond breakages is a function of their relative bond strengths. For this reason, LPE nanosheets (such as those investigated here) have consistent aspect ratios of length-to-thickness and length-to-width.

When discussing 2D nanosheets, it is also more useful to consider the layer number, N, rather than absolute thickness. Using the crystallographic thickness (d_0), the nanosheet thickness (h) in the previous expression can be replaced by $h = Nd_0$. Additionally, we write the mean aspect ratios as length to thickness, $k_{Lt} = \langle L/h \rangle$, and length to width, $k_{lw} = \langle L/W \rangle$. Then we model the 2D nanosheets as rhombohedral prisms of length, L, and width, W, such that nanosheet area is $A = LW/2$. Rearranging Equation (6), and writing A in terms of h via the aspect ratios allows us to reduce the dimensionality of the sedimentation coefficient, such that Equation (6) becomes:

$$\ln\left(\frac{r}{r_0}\right) = \frac{(Nd_0)^2(\rho_{NS} - \rho_l) + 2dNd_0(\rho_s - \rho_l)}{10.5\eta\frac{\sqrt{k_{lw}}}{k_{Lt}}}\omega^2 t \qquad (7)$$

Plotting Equation (7) for rhombohedral nanosheets using the parameters in Table 1 against a conventional hard sphere approximation (Equation S2), in Figure 1D, clearly highlights the importance of accurately describing nanoplatelet shape. The rhombohedral model was found to be accurate over a range of centrifuge speeds and conditions for WS_2, MoS_2, and graphene, shown in Figure 1E–G. As expected, at higher rotation speeds the nanosheets sink faster allowing greater separation of thinner sheets. We also note that the lower density of graphene sheets required much higher rotation speeds to achieve a similar sheet separation.

When modeling low-density nanosheets such as graphene (or hBN), to maximize accuracy, it is important to include the surfactant layer in the effective density. Estimates for surfactant density and surfactant layer thickness (ρ_S = 1595 kg m^{-3}, d = 4.25 Å) were taken from an analytical ultracentrifugation study on single-walled carbon nanotubes [33]. Since carbon nanotubes have similar surface properties to graphene we find good agreement with our experimental data. Plotting Equation (7) for graphene neglecting the surfactant, i.e., setting $\Delta\rho_S$ to zero, predicts a slightly slower sedimentation than experimentally measured, illustrated in Figure 1G. However, excluding this surfactant contribution makes little difference to the predicted movement of high-density TMDCs, as illustrated for MoS_2 in Figure 1F, where Equation (7) is plotted with and without surfactant.

It is possible that nanosheets with exceptionally high chemical inhomogeneity may alter nanosheet and hydration layer density enough to make a difference. Since the complete omission of SC surfactant from TMDCs does not significantly impact the sedimentation rate, we expect this threshold to be high (except for low-density materials such as graphene and hBN). Nonetheless, it should be acknowledged that polymeric surfactants were reported to significantly lower the buoyant density of TMDCs [18]. This will likely be reflected in slower sedimentation. Here, it will be important to experimentally and theoretically extend our knowledge on surfactant adsorption to be able to estimate buoyant densities and surfactant layer thicknesses for a broader range of additives in the future.

The rigid shape of the nanosheets is a further prerequisite for an accurate modeling of the sedimentation. For nanosheets of aspect ratios characteristic for sonication/shear-assisted LPE and high rigidity modulus, this assumption is clearly valid. As described below, we tested the model for seven types of LPE nanosheets and find good agreement between experiment and theory in all cases. However, it should be noted that the creation of larger area nanosheets is an ongoing aim within the community and more flexible sheets may exhibit bending or folding into a more spherical shape with lower viscous resistance than expected from our model. This limit is currently unknown. Since that behavior would be an important parameter for printing and coatings, this model may offer one possible method for testing such phenomena.

Within the limits imposed by the assumptions required to make the mathematics tractable pointed out above, these band sedimentation experiments validate our size and shape model for nanosheet motion.

2.3 | Population Distributions in Sediment and Supernatant

With an accurate model to describe the sedimentation coefficient of 2D nanosheets, it is possible to calculate the relative motion of a

TABLE 1 | Relevant parameters of the materials used for band sedimentation experiments. Nanosheet aspect ratios were determined from AFM statistics and averaged over all nanosheets counted in the context of ref. [50]. Solvent density and viscosity used were $\eta = 7.8 \times 10^{-4}$ kg m^{-1} s^{-1} and $\rho_l =$ 1060 kg m^{-3} based on average composition [51], see Section S4.1 for details.

Materials	ρ / kg m^{-3}	d_0 / Å	k_{lw}	k_{Lt}
Graphene	2260	3.5	2.4	180
WS_2	7500	6.3	1.7	46
MoS_2	5060	6.2	1.8	49

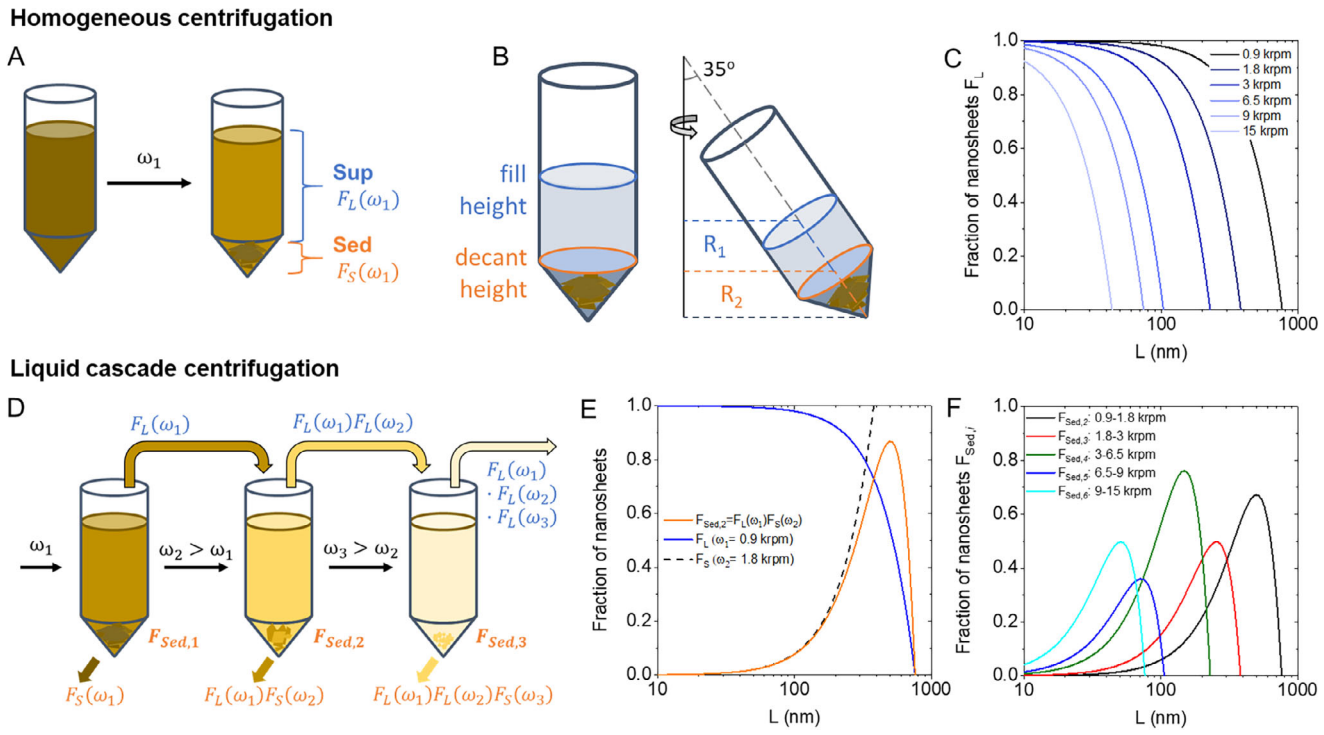

FIGURE 2 | Description of commonly applied centrifugation schemes in fixed-angle rotors. A) Schematic of a single-step homogeneous centrifugation resulting in a supernatant and sediment which are a function of angular frequency and time. B) Schematic of a centrifuge tube in a fixed-angle rotor with the relevant radii. C) Fraction of nanosheets (as function of length) remaining in the supernatant after centrifugation (F_L) at angular frequencies predicted by theory (WS_2, H_2O, 10°C, 2 h). D) Schematic of liquid cascade centrifugation with sequentially increasing centrifugation speeds. Sediments after each step are collected for analysis and supernatants subjected to the next step at higher speeds. From the second step onward, the nanosheet size in the sediment is determined by the angular frequency of all proceeding steps. For example, the fraction of Sed3 is $F_L(\omega_1)F_L(\omega_2)F_S(\omega_3)$. E) Fraction of nanosheets (as function of length) of a supernatant (F_L) after 0.9 krpm and a sediment (F_S) after 1.8 krpm compared to the fraction of nanosheets obtained in a sediment when using these angular velocities as lower and upper centrifugation boundary. F) Fraction of nanosheets (as function of length) in sediments collected in a typical LCC experiments as used in this work (WS_2, H_2O, 10°C, 2 h). For E) and F) the typical experimental parameters in Tables 1 and 2 are used as input, as well as d = 0.43 nm and $\Delta\rho_S = 530$ kgm^{-3}.

particle from a known starting position in a swinging bucket rotor. However, centrifugation is more commonly used on nanosheets homogeneously distributed throughout the centrifuge tube prior to centrifugation to separate a sediment, sometimes termed a pellet, at the bottom of the tube from the supernatant remaining above, illustrated in Figure 2A. We term this simple single step scenario homogeneous centrifugation to distinguish between different alternatives.

To describe this separation of sediment from supernatant we must define a specific height to delineate these two phases. We acknowledge that for many real samples the distinction between solid sediment and liquid supernatant can be ill-defined, but throughout many experiments we find good results are obtained when using the height of the narrower base of the tube as the decanting height, especially since this is a feature of most centrifuge tubes.

The angle of the tube relative to the plane of rotation must also be considered since many commercial centrifuges use fixed-angle rotors, as these allow for higher speeds and are more stable towards vibrations. This design takes advantage of the Boycott effect, where a depleted layer of lower concentration fluid forms on the inside edge of the tube generating an additional current driving accelerated sedimentation [52]. Different corrections of the sedimentation coefficient have been proposed to account for this, however they require complex analysis of centrifuge tube size, shape, and geometry and cannot be uniformly applied

across experiments [53–55]. Fortunately, despite neglecting this influence here, good results are obtained for all samples tested, as will be demonstrated below. We therefore need only resolve the geometry of the centrifuge tube to ensure the distance from the radius is accurately described from by the vertical fill height. This simple geometry correction is shown in Figure 2B, along with the labeled radii to the top of the liquid, R_1, and the decanting point, R_2, where we delineate the supernatant from the sediment.

To find the population of sheets that sink into the sediment, we can use the equations of motion working backwards from the decanting point, R_2. Using the sedimentation rate defined above in Equation (6), the distance the nanoplate has traveled from an initial position, r_0 in time t is:

$$\Delta r = r - r_0 = r_0\left(e^{S\omega^2 t} - 1\right) \tag{8}$$

Setting the final position, r, of the sheet to R_2, we can calculate the initial position (which we term $r = r_{sed}$) from which a nanosheet will migrate exactly to the decanting point by the end of the centrifuge experiment. Further, since we know $\Delta r \propto r_0$, any sheets that start at larger r_0, that is sheets found further down the tube, will travel an even greater distance and must finish the experiment past the decanting point, also in the sediment.

Thus, r_{sed} is a threshold, above which any sheets at $t = 0$ will remain in the supernatant, whilst any sheets at or below this point will terminate in the sediment. If the nanosheets are homogeneously distributed at the start of the experiment, the relative population of sheets in the sediment, F_S and supernatant, F_L, is then found by the relative amounts of solution above and below r_{sed}, as given in Equation (9):

$$F_L(A,h,\omega,t) = \begin{cases} \frac{R_2 e^{-S\omega^2 t} - R_1}{R_2 - R_1}, & S\omega^2 t \le \ln\left(\frac{R_2}{R_1}\right) \\ 0, & S\omega^2 t \ge \ln\left(\frac{R_2}{R_1}\right) \end{cases} \tag{9}$$

We note that, by definition, $F_S + F_L = 1$. The smooth change in function allows us to account for the finite length and fill height of the centrifuge tube. In the limiting case, the maximum distance any particle can sink is from the top of the liquid, R_1, to the base of the centrifuge tube, $\approx R_2$; we find this condition is met when $S\omega^2 t = \ln(R_2/R_1)$. For sheets sinking faster than this, the top expression predicts they will pass through the bottom of the centrifuge tube. This is clearly impossible, but we can safely assert that $F_{liq} = 0$ for any nanosheet beyond this limit since all values of r_0 will terminate in the sediment. A complete derivation of this expression and limiting conditions is found in Section S2.2.

To visualize this trend, we use the same mean aspect ratio approximations described for the band sedimentation experiment, except we now define S exclusively in terms of sheet length, L. In addition, neglecting surfactant for simplicity (i.e., setting $\Delta\rho_S$ to zero) yields:

$$S(L) = \frac{\Delta\rho_{NS} L^2}{10.5\eta k_{Lt}\sqrt{k_{lw}}} \tag{10}$$

We can then combine Equations (9) and (10) to plot the population fraction remaining in the supernatant, F_L, as a function of nanosheet length, L, in Figure 2C. Here we consider WS_2 in water at 10°C for 2 h at various rotation speeds, modeling the effect of typical centrifuge preparation conditions reported previously. This shows that, because very small nanoplatelets have a low velocity, their population remains relatively unchanged by the centrifugation. As the platelet size increases, the fraction remaining decrease sharply to zero, the limiting case above which all nanosheets will sink completely into the sediment.

This plot also demonstrates the trend from increasing the rotation speed. As expected, at higher speeds the particles are accelerated to a higher velocity, so a greater fraction of them sink into the sediment during the time interval of the centrifugation and the curve and x-intercept move to smaller nanosheet length. This observation was the conceptual basis of liquid cascade centrifugation [20] which is illustrated in Figure 2D: a cascade of sequentially increasing rotation speeds allows selection of decreasing nanosheet sizes. While more time-consuming than a single centrifuge separation, the strength of LCC is the distinct and narrow size distribution obtained in each step, allowing investigations of size-dependent properties.

Crucial to the "cascade" of LCC is applying the sequentially increasing speeds (or times) to the supernatant from the previous step. In that way those larger sheets, which sediment at lower speeds, are removed during the initial steps while very small sheets, that require higher speeds to enter the sediment in a given time, will remain longer in the supernatant and only sink to the sediment in later steps of the cascade.

To model an LCC process, each new fraction is a product of all previous centrifuge separations that sample has been subjected to. To illustrate this, a simple three step cascade is shown in Figure 2D. In such a cascade, after the first centrifugation step (at ω_1), large unwanted material is sent to the sediment while the supernatant is collected. The fraction of nanosheets in this supernatant is then $F_L(\omega_1)$. In the second step, the supernatant is centrifuged again (at $\omega_2 > \omega_1$). The resultant sediment and supernatant are then collected. The fraction of nanosheets in each are given by $F_L(\omega_1)F_s(\omega_2)$ and $F_L(\omega_1)F_L(\omega_2)$ respectively. In the third step, the process is repeated again and the fraction of nanosheets in sediment and supernatant are given by $F_L(\omega_1)F_L(\omega_2)F_s(\omega_3)$ and $F_L(\omega_1)F_L(\omega_2)F_L(\omega_3)$ respectively. We note that the desired size-selected nanosheets are collected in each sediment with nanosheet size decreasing with step number. For a cascade with many steps, the fraction of nanosheets in the i^{th} sediment is expressed as:

$$F_{Sed,i} = F_S(\omega_i)\Pi_{j=1}^{i-1} F_L(\omega_j) \tag{11}$$

However, we note that higher speed centrifuge processes always sediment more material than lower speeds. We can then safely neglect all but the final two steps, considering only the supernatant from the second last step and the sediment obtained at the highest rotation speed:

$$F_{Sed,i} \approx F_L(\omega_{i-1})F_S(\omega_i) = F_L(\omega_{i-1})(1 - F_L(\omega_i)) \tag{12}$$

Any pair of adjacent centrifugation steps (e.g., ω_i and ω_{i-1}) effectively slice the initial polydisperse nanosheet size distribution. The first step will exclude any sheets larger than the cut-off while the second step minimizes the population of smaller nanoplatelets that sink too slowly to enter the sediment. This is shown in Figure 2E, where the fraction of nanosheets remaining in the supernatant after a low-speed centrifugation (specifically 0.9 krpm) is plotted as a function of nanosheet length along with the fraction of nanosheets that sediment at higher speeds (specifically 1.8 krpm). The fraction of nanosheets collected as sediment trapped between this pair of centrifugation speeds is the product of both functions in Equation (12).

For these illustrations, we plot line graphs of the fractional population change with sheet length. However, it must be noted that the full form of this function is a multidimensional surface over all nanosheet dimensions: L, W & N (or h). Figure S5 illustrates this by showing a 2D surface of the fractional population change with L & N since any higher dimensions cannot be easily visualized. Applying the mean aspect ratio approximation is equivalent to taking a slice out of the 3D function in Figure S5 along a plane defined by $h = L/k_{Lt}$. This is defined by the path of most probable nanosheet sizes found in the original distribution, as described by the thermodynamics of LPE [50].

We note that a fully rigorous analysis requires consideration of the starting nanosheet size distribution which would be a correlated three-dimensional log-normal distribution parameterized by nanosheet length, width, and height [36]. We refer to such a distribution as $P_{stock}(N,L,W)$ and the complete form of this is found in Equation S4. If this distribution was known, the exact population of all nanosheet sizes, P, resulting from centrifugation could be predicted by mapping the stock distribution function to the population change function (i.e., F_S or F_L) for every L, N, and W:

$$P_{Sed,i}(N,L,W) = P_{stock}(N,L,W)\,F_{Sed,i}(N,L,W) \tag{13}$$

In principle, if the L, N, and W distributions were measured in finely separated fractions, the size distribution in the stock prior to centrifugation could be reconstructed. Likewise, the population change function could be equally applied to a volume or mass distribution, were such a population known for the starting material. These will be very different to the number population, but in principle accessible within the framework of the model.

However, unfortunately, the full population distribution of a stock directly from exfoliation has not yet been measured. Difficulties arise due to the wide range of particles sizes that must be accurately measured, in large enough numbers to be statistically significant, and without any bias towards smaller or larger sheets. In spite of advances in automated image analysis [56, 57], current microscopy methods such as atomic force microscopy (AFM) cannot resolve the smallest and largest nanosheets simultaneously to enable such an unbiased count, and spectroscopic methods are only sufficient to measure averaged values. Example images of such stock samples for WS_2 exfoliated in aqueous sodium cholate and N-methyl-pyrrolidone (NMP) are shown in Figures S12 and S13 to illustrate this issue.

Fortunately, we find that if suitable centrifuge conditions are used—specifically small steps between rotation speed sizes, the resulting population in the sediment ($F_{sed,i}$) is much narrower than the stock distribution (P_{stock}), allowing us to treat the unknown stock distribution function as constant:

$$P_{Sed,i}(N,L,W) \propto F_{Sed,i}(N,L,W) \tag{14}$$

Such narrow steps are limiting for very crude processing, but in previous investigations on LCC [50], we have identified near-optimum conditions to balance the number of steps in the cascade with well-defined sheet sizes in each fraction. The fraction of nanosheets in each sediment obtained from such a cascade is calculated using our new theoretical framework (Equations 9, 10, 12) as shown in Figure 2F, again using the mean aspect ratio approximation to produce a 2D line plot of $F_{Sed,i}$ versus L for i = 2,3,4,5,6. From the plot in Figure 2F, two key features can be observed as the angular rotation speed is increased: firstly, the maximum size decreases as the nanosheets sediment faster; secondly, in every case, a well-defined peak in the distribution is observed. These offer measurable size values that will allow to predict the centrifugation process as outlined below, and thereby test the validity of our assumptions regarding the sedimentation of nanosheets. We note that, this form of the model does not account for minor effects such as shape filtering, e.g., changes in length-width aspect ratios with centrifugation that have been observed previously [50, 58].

2.4 | Calculating Representative Nanosheet Sizes and Comparing with Experiment

To test the applicability of our model to LCC data, we prepared a set of four nanosheet samples using the cascade centrifugation conditions shown in Figure 2F. To be able to assess the accuracy of the theoretical framework for sedimentation in different liquid environments, it was important to subject identical samples to centrifugation, but in different solvents. While the average nanosheet aspect ratios are primarily governed by the binding and tearing energies of the bulk material [50], it has been reported that changes in the nanosheet population in different fractions after LCC can be observed when comparing, for example, graphite exfoliated in aqueous sodium cholate versus NMP, respectively [50]. To date, it was not clear whether this was an effect of centrifugation or the presence of different particle size distributions from exfoliation in surfactant versus solvent. To address this, WS_2 was exfoliated in both aqueous SC and NMP by sonication-assisted LPE. We chose WS_2 as model substance due to its high density that allows us to neglect contributions from the surfactant to the effective density. The as-sonicated dispersions were split into two aliquots, and each transferred to both solvents systems through high-speed centrifugation followed by redispersion, resulting in four stock dispersions that were subjected to LCC and the size distributions measured through AFM statistics (see Section S5). Note that the scatter plots of length versus nanosheet layer number in Figure S20 demonstrate that different nanosheet size distributions and even slightly different nanosheet length-thickness aspect ratios are obtained from exfoliation in surfactant versus solvent.

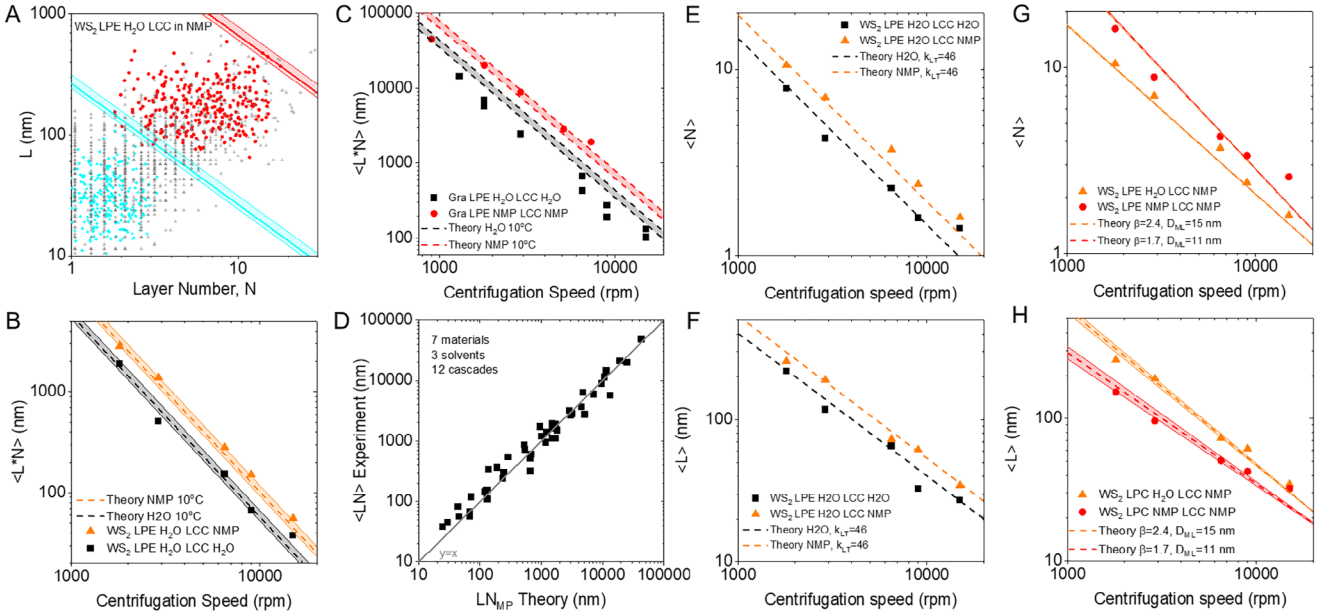

FIGURE 3 | Comparison of experiment and theory in LCC. A) Nanosheet sizes as measured by AFM of two WS_2 LCC fractions (WS_2 exfoliated in aqueous sodium cholate (SC) and centrifuged in NMP), with predicted maximum sheet size limits shown as diagonal lines. The shaded area around the lines show the confidence interval from the observed range of aspect ratios across the LPE-derived nanosheets measured [50, 58–61]. B,C) Arithmetic mean of the product of length and layer number, ⟨LN⟩, in size-selected fractions as function of sediment angular velocity for B) WS_2 and C) graphene centrifuged in aqueous SC and NMP, respectively. The graphene data is originally from ref. [50]. Shaded areas show confidence intervals from the observed range of aspect ratios across the LPE-derived nanosheets measured [50, 58–61]. D) Comparison of experimental and theoretical ⟨LN⟩ from all data analyzed (see Supporting Information). E,F) Arithmetic mean layer number (E) and length (F) as function of angular velocity of LCC size-selected WS_2 exfoliated in aqueous SC. Dashed lines represent theory using the mean aspect ratio approximation. G,H) Arithmetic mean layer number (G) and length (H) as function of angular velocity of WS_2 centrifuged in NMP, exfoliated in SC and NMP, respectively showing different exponents relating ⟨N⟩ and ⟨L⟩ to the angular velocity. These can be accounted for theoretically (Equations 20 and 21, dashed lines) when using the actual exponents, β, relating ⟨L⟩ and ⟨N⟩ and experimental values for the characteristic monolayer length D_{ML}. Shaded areas denote the confidence interval estimated from the errors of fitted values in ref. [50]

To compare experiment and theory, we calculate the maximum possible nanosheet length observable within a given fraction. To do this, we use our model (see Section S2.5) to calculate the nanosheet length where $F_{Sed,i} = 0$. We refer to this as the upper cut-off length, L_{cut}, which depends on layer number, N, as follows:

$$L_{cut} = \frac{10.5\eta\sqrt{k_{lw}}}{\omega_{i-1}^2 t\,(Nd_0\Delta\rho_{NS} + 2d\Delta\rho_S)} \ln\left(\frac{R_2}{R_1}\right) \quad (15)$$

here, the appropriate angular frequency is that used to generate the supernatant that was then centrifuged to give the sediment, i.e., ω_{i-1}, since this step was where the larger flakes were excluded. This cut-off function is plotted over the L-N scatter plot of sheets measured from AFM of WS_2 exfoliated in aqueous SC and centrifuged in NMP in Figure 3A. Only two fractions are shown here for clarity, but full plots of all LCC fractions over the four samples mentioned above are shown in Figure S21. The measured sheet sizes are widely scattered below this cut but, over 12 different fractions, no data points are observed above the lines representing the predicted maximum. This supports the validity of Equation (15) and the model underlying it.

The sharp peaks observed in the population distributions after cascade centrifugation in Figure 2F suggest it is also possible to calculate the most probable nanosheet size in each fraction. This parameter turns out to be a useful estimate of the mean nanosheet size for well-chosen size selection procedures. By differentiating $F_{sed}(N,L)$ with respect to LN we find an expression that, so long as the difference in speed between the steps is kept small, can be solved (see Section S2.6). This yields an equation for the most probable value of LN:

$$(LN)_{MP} \approx \frac{10.5\eta\sqrt{k_{lw}}}{\omega_i^2 t d_0 \Delta\rho_{NS}} \ln\left(\frac{2R_2}{R_2 + R_1}\right) \approx \langle LN\rangle \quad (16)$$

This expression includes experimental parameters that could be varied to access a desired nanosheet size, most usually ω_i but also t. We reiterate that here, the appropriate angular frequency is that used to generate the sediment which contained the nanosheets in question (i.e., ω_i, see Section S6.2). The material-dependent information required also includes some knowledge of k_{lw}, the length-width aspect ratio of nanosheets. For most commonly used 2D materials prepared by LPE this has been shown to lie within a narrow range (1.5–2.5) [50, 58–61]. Further guidance on the practical use of this equation is available in Section S2.6. An excel sheet to calculate centrifugation conditions for desired nanosheet size and thickness is also provided in Supporting Information document [web app calculator].

Comparing ⟨LN⟩ for WS_2 and graphene size-separated by LCC in water and NMP, shown in Figure 3B,C, we see good agreement between the prediction of the most probable size (using input

TABLE 2 | Experimental parameters of the LCC, and solvent properties at 10°C.

Standard LCC	
R_1 (mm)	75
R_2 (mm)	93
Time (s)	7200
Temperature	~10°C
Rotation Speed (krpm)	0.9, 1.8, 3, 6.5, 9, 15

Solvents	**Density (kg m^{-3})**	**Viscosity (kg m^{-1} s^{-1})**
H_2O + sodium $cholate_{(aq)}$	1000	0.0013
NMP	1030	0.0023

parameters from Table 2) and the mean size as measured by AFM. The discrepancy found for graphene centrifuged in water is most likely due to the surfactant coating. In NMP, this coating is removed, replaced by the solvent, however, as seen from band sedimentation for low-density materials such as graphene, this surfactant can be a significant contribution to the effective density in aqueous dispersions (which was neglected for Equation 16 to simplify the expressions).

Considering a wider comparison of eight different materials: WS_2 (this work, Section S5), graphene [50], MoS_2 [50], hBN [62], GaS [50], $Cu(OH)_2$ [63], $NiPS_3$ [61], $CrTe_3$ [60]; prepared in three solvents: aqueous sodium cholate, NMP and N-Cyclohexyl-2-pyrrolidone (CHP), and size-selected with 12 LCC experiments from previously published literature, we show the model derived in this work accurately predicts the mean sheet sizes $\langle LN \rangle$ across the materials and experiments tested. This is summarized by the plot Figure 3D which shows the measured, experimental $\langle LN \rangle$ as function of calculated most probable nanosheet size. Here, each data point is the average of one LCC size-selected fraction (but excluding low-density materials such as graphene and hBN in aqueous surfactant solution). Full data sets and detailed comparison between experiment and theory for all materials are found in Section S7. This illustrates that our model can be used to predict $\langle LN \rangle$.

Without a more complete knowledge of the nanosheet size distribution in the stock dispersion, these predictions are limited to number populations, and cannot be extended to mass or volume-weighted distributions which can be of interest for real-world manufacturing. It is clear that much of the initial particle mass is lost in the first purification steps where large/thick sheets are extracted. While this is more a question of production yield rather than purification, it would be interesting to be able to predict mass or volume-weighted distributions. While the change in particle size distribution, F_i, can equally be applied to a number or volume-weighted population function, the sharp peaks in number density (that result from narrow cascade steps) will underestimate the contribution of even small numbers of large flakes that can have a significant impact on the volume-weighted distribution. In contrast, any attempt to blindly account for volume, without somehow constraining flake sizes present in the initial dispersion as a result of their production method, is likely to lead to an overestimation of the largest flakes irrespective of the feasibility of producing them. For LPE nanosheets which are known to have relatively constant aspect ratios [50], we note that it was observed that number and volume-fraction weighted averages are related to each other and can be described by the same empirical function across different materials (see Figure S30 of ref. [50]). In such a case, the prediction of number averages is sufficient. Further, the aspect ratios can be used to derive equations to predict $\langle L \rangle$ and $\langle N \rangle$, as discussed below.

2.5 | The Mean Aspect Ratio Approximation

An accurate prediction of $\langle LN \rangle$ is useful, but it would be even more interesting to directly predict $\langle L \rangle$ and $\langle N \rangle$ separately. We can achieve this by relating $\langle L \rangle$ and $\langle N \rangle$ via mean aspect ratio. As mentioned above, we have used $k_{Lt} = \langle L/h \rangle$. We can approximate this as $k_{Lt} \approx \langle L \rangle / d_0 \langle N \rangle$. Then approximating $\langle LN \rangle \approx \langle L \rangle \langle N \rangle$ and using the result above to replace either $\langle L \rangle$ or $\langle N \rangle$ yields equations which allow mean sheet length and layer number to also be calculated separately:

$$L_{MP} \approx \left(\frac{10.5\eta\sqrt{k_{lw}}k_{Lt}}{t\Delta\rho_{NS}} \ln\left(\frac{2R_2}{R_2+R_1}\right)\right)^{1/2} \frac{1}{\omega_i} \approx \langle L \rangle \tag{17}$$

And

$$N_{MP} \approx \left(\frac{10.5\eta\sqrt{k_{lw}}}{tk_{Lt}d_0^2\Delta\rho_{NS}} \ln\left(\frac{2R_2}{R_2+R_1}\right)\right)^{1/2} \frac{1}{\omega_i} \approx \langle N \rangle \tag{18}$$

We note that Equations (17) and (18) use the approximation that the length-thickness aspect ratios of LPE nanosheets are well-defined with a narrow distribution around a constant value. To test these expressions, the experimental $\langle N \rangle$ and $\langle L \rangle$ from AFM analysis is plotted against the centrifugation speed in Figure 3E,F for WS_2 exfoliated in aqueous SC and centrifuged both in aqueous SC, and NMP, and shows good agreement with the theoretical prediction. However, we note that the experimental results from the NMP-exfoliated WS_2 deviate somewhat from the theoretical prediction (Figure S25).

However, since the decoupling of the effect of exfoliation and centrifugation on nanosheet lateral size and thickness in solvent versus surfactant media performed here clearly shows that aspect ratios can be different for exfoliation in surfactant and solvent (Figure S24), we expect that there are some restrictions to the mean aspect ratio approximation, i.e., restrictions to Equations (17) and (18) (but not Equation 16), that we will analyze in detail.

2.6 | Beyond the Mean Aspect Ratio Approximation

The comparison of WS_2 exfoliated in aqueous SC and NMP, respectively, demonstrates that this mean aspect ratio approximation is not always fully accurate. This is because aspect ratios of

nanosheets within a dispersion also provide information about the production and history of the sample. To address this, we now extend our model to a more accurate representation of the nanosheet size distributions. We make use of an expression we found previously which showed that for LPE-produced nanosheets there is a power-law dependence between the lateral sheet size and thickness [50].

$$\langle LW \rangle = D_{ML}^2 \langle N \rangle^{\beta} \tag{19}$$

where D_{ML} is the characteristic monolayer size and β is a constant in the range 1.5–3, being typically centered at ~2.8 (Section S7). Using this relation in place of the mean aspect ratio for most probable nanosheet size, Equations S10 and S11 can be derived, which show that

$$\langle N \rangle \approx \left(\frac{10.5\eta}{t d_0 \Delta\rho_{NS} D_{ML}} \ln\left(\frac{2R_2}{R_2 + R_1} \right) \right)^{1/(1+\beta/2)} \frac{1}{\omega_i^{1-(\beta-2)/(\beta+2)}} \tag{20}$$

$$\langle L \rangle \approx \sqrt{k_{wl}} D_{ML} \left(\frac{10.5\eta}{t d_0 \Delta\rho_{NS} D_{ML}} \ln\left(\frac{2R_2}{R_2 + R_1} \right) \right)^{\beta/(2+\beta)} \frac{1}{\omega_i^{1+(\beta-2)/(\beta+2)}} \tag{21}$$

We note that the values of $(\beta - 2)/(\beta + 2)$ are generally quite small such that the deviations from the behavior predicted by Equations (17) and (18), although observable, are not significant.

Exfoliating nanosheets in water and NMP has been observed to produce dispersions with different β (but similar D_{ML}) values in the case of graphene [50]. We have confirmed this result here via more elaborated experiments using WS_2, where the effect of the solvent on exfoliation and centrifugation was decoupled in contrast to the previous work on graphene (see Figure S26A–D). Figure 3G,H plots $\langle N \rangle$ and $\langle L \rangle$ versus ω_i for the two WS_2 sample sets that were exfoliated in different media (but both centrifuged in NMP). These graphs clearly show angular frequency dependence that deviate slightly from the $1/\omega_i$ behavior predicted by Equations (17) and (18). However, the measured behavior can be reproduced by plotting Equations (20) and (21) over the data (dashed lines) using the experimental parameters (Table 2) and the measured values of β and D_{ML} given in the panel (see Figure S27 for measurements). We emphasize the excellent agreement between theory and data. We note that such differences in exponent have been reported on previously but were not explained [60–62]. We can now show that such differences are not due to any difference in behavior within the centrifugal field, but rather it is a result of the difference in the statistical distribution of sheet sizes in the stock caused by different production methods.

In the cases studied here, the difference in aspect ratio was known from AFM-derived statistics, but such large datasets remain time-consuming to obtain. Our new understanding of the difference in exponent suggests it may be possible to estimate such mechanistic differences between exfoliation methods from centrifugation data sets in future, in addition to predicting mean nanosheet sizes.

3 | Conclusion

We have derived a model for the sedimentation of 2D nanosheets within a centrifugal field, combining a rhombohedral model for sheet density with an oblate spheroid model for viscous resistance. Rate zonal sedimentation experiments have shown the reliability of sedimentation coefficients calculated from this model without needing to complete prior experiments to determine empirical correction factors. Using these sedimentation coefficients, we show it is possible to predict individual nanosheet motion, and also to extend this to predict changes in the relative populations of nanosheets in bulk dispersions. Even without knowledge of a complete size distribution function of the stock dispersion, key metrics (cut size, average nanosheet size) can be predicted so long as the size-selection window is sufficiently narrow to overwhelm the inherent dispersity of the stock. This is experimentally verified from a range of nanosheet dispersions size-selected through LCC. Such predictions relating to size distribution functions can in principle be applied to other particle shapes and sizes. The use of aspect ratios to reduce the dimensionality of the 2D nanosheet problem also offers information about underlying exfoliation mechanisms. In future, analytical centrifuge experiments may provide greater insights to nanosheet size distributions and production methods. Conversely, it may also be instructive to test the limits of these models by using colloidally stable 2D materials that do not require LPE, like talc or laponite, or to investigate electrochemically-exfoliated 2D materials which have larger, less well-defined length-thickness aspect ratios. The ability to predict population changes during centrifugation also allows much greater optimization of size selection procedures, where specific sheet sizes can be tailored to applications and meaningful comparisons can be made between different material and solvent systems independent of extrinsic size effects caused by purification.

4 | Methods

A detailed method section is found in Section S3.

4.1 | Preparation of the Dispersion

Graphite and group VI-TMDC dispersions were prepared by probe sonicating the powder according to previously published methods [50]. In brief, a two-step sonication was used. The initial 1 h sonication was used to purify the commercial powder to remove impurities in the supernatant after centrifugation, while the sediment was subjected to 5 h sonication to prepare the stock dispersions used for size selection.

4.2 | Band Sedimentation

For band sedimentation, 1 g L^{-1} SC was dissolved in H_2O/D_2O. As bottom layer, 100% D_2O was used, followed by layering 50/50 vol.% H_2O/D_2O on top and finally the nanomaterial dispersion. Band sedimentation was performed in swinging bucket rotors for the speeds and time indicated in the figures. After centrifuging the samples were immediately subjected to fractionation and bands removed in 1 mL aliquots using a needle

and syringe. dius values were measured for each aliquot from the rotor and tube height. A limited initial size selection was used for all samples prior to band sedimentation experiments as detailed in the Supporting Information.

4.3 | Liquid Cascade Centrifugation

The WS_2 dispersions in NMP and SC, respectively, were each split into two equal aliquots and centrifuged at 15 krpm for 3 h. The sediments were redispersed in water and centrifuged again at 15 krpm. After this step, half of each dispersion was redispersed in SC (2 g L^{-1}) and half in NMP resulting in four stock dispersions subjected to LCC. While different centrifuges and rotors were used in this experiment, we note that relevant parameters were similar ($R_1 = 75$ mm and $R_2 = 93$ mm). For the WS_2 data shown in the main manuscript, all centrifugation runs were performed for 2 h (10°C).

Unexfoliated material was removed by centrifugation at 900 rpm. The supernatant was subjected to further centrifugation at 1.8 krpm. The sediment was collected in fresh surfactant, while the supernatant was centrifuged at 2.9 rpm. Again, the sediment was collected and the supernatant subjected to centrifugation at higher speeds. This procedure was repeated with the following centrifugation speeds: 6.5, 9, and 15 krpm. As sample nomenclature, the lower and upper boundary of the centrifugation are indicated.

Additional LCC data for other materials analyzed in the Supporting Information is published data.

4.4 | UV/VIS Extinction Spectroscopy

UV/VIS extinction spectra were recorded using 0.5 nm data intervals in quartz glass cuvettes. Where required, samples were diluted into a sodium cholate solution.

4.5 | Atomic Force Microscopy

Atomic force microscopy was carried out on a Dimension ICON3 scanning probe microscope (Bruker AXS S.A.S.) in ScanAsyst in air under ambient conditions using aluminium-coated silicon cantilevers after deposition on Si/SiO_2 coated with (3-Aminopropyl)triethoxysilane. Typical image sizes ranged from 20 × 20 for larger nanosheets to 3 × 3 μm^2 at scan rates of 0.5–0.8 Hz with 1024 lines per image. Previously published step height was used to convert apparent thickness to layer number [20] and corrections were used to correct lateral dimensions from cantilever broadening [64].

Acknowledgements

We acknowledge funding from the European Union through the 2D-PRINTABLE project (GA-101135196) and thank Jana Zaumseil for the access to the infrastructure at the Chair of Applied Physical Chemistry. V.V.-M. acknowledges grants TED2021-131906A-100 and RYC2022-035200-I funded by the Spanish Ministry of Science, Innovation and Universities and support from the Regional Government of Madrid (2024-T1/TEC-31349).

Conflicts of Interest

The authors declare no conflicts of interest.

Author Contributions

S.G. performed and evaluated band sedimentation, S.O. and T.S. performed LCC and AFM of WS_2, S.G., A.D., C.G., V.V-M., and J.N.C. developed theoretical analysis, K.S. performed AFM, M.H. performed and evaluated rheology, J.N.C. derived the theory, C.B. evaluated AFM and analyzed LCC data, J.N.C. and C.B. conceptualized the work, S.G., J.N.C., and C.B. wrote the manuscript.

Data Availability Statement

The data that support the findings of this study are available from the corresponding author upon reasonable request.

References

1. A. G. Kelly, D. O'Suilleabhain, C. Gabbett, and J. N. Coleman, "The Electrical Conductivity of Solution-Processed Nanosheet Networks," *Nature Reviews Materials* 7 (2022): 217–234, https://doi.org/10.1038/s41578-021-00386-w.

2. R. Yang, J. Zhou, C. Yang, L. Qiu, and H. Cheng, "Recent Progress in 3D Printing of 2D Material-Based Macrostructures," *Advanced Materials Technologies* 5 (2020): 1901066, https://doi.org/10.1002/admt.201901066.

3. M. Cai, J. Yang, X. Lu, and X. Lu, "Layer-by-Layer Self-Assembly Strategies of Atomically Thin Two-Dimensional Nanomaterials: Principles, Methods, and Functional Applications," *ACS Applied Nano Materials* 7 (2024), 27940–27959, https://doi.org/10.1021/acsanm.3c06286.

4. J. Azadmanjiri, P. Kumar, V. K. Srivastava, and Z. Sofer, "Surface Functionalization of 2D Transition Metal Oxides and Dichalcogenides via Covalent and Non-covalent Bonding for Sustainable Energy and Biomedical Applications," *ACS Applied Nano Materials* 3, (2020) 3116–3143, https://doi.org/10.1021/acsanm.0c00120.

5. T.-H. Le, Y. Oh, H. Kim, and H. Yoon, "Exfoliation of 2D Materials for Energy and Environmental Applications," *Chemistry—A European Journal* 26 (2020): 6360–6401, https://doi.org/10.1002/chem.202000223.

6. J. Liu, D. Hui, and D. Lau, "Two-Dimensional Nanomaterial-Based Polymer Composites: Fundamentals and Applications," *Nanotechnology Reviews* 11 (2022): 770–792, https://doi.org/10.1515/ntrev-2022-0041.

7. Z. Li, R. J. Young, C. Backes, et al., "Mechanisms of Liquid-Phase Exfoliation for the Production of Graphene," *ACS Nano* 14 (2020): 10976–10985, https://doi.org/10.1021/acsnano.0c03916.

8. K. R. Paton, E. Varrla, C. Backes, et al., "Scalable Production of Large Quantities of Defect-Free Few-Layer Graphene by Shear Exfoliation in Liquids," *Nature Materials* 13 (2014): 624–630, https://doi.org/10.1038/nmat3944.

9. M. Zhao, C. Casiraghi, and K. Parvez, "Electrochemical Exfoliation of 2D Materials Beyond Graphene," *Chemical Society Reviews* 53 (2024): 3036–3064, https://doi.org/10.1039/D3CS00815K.

10. R. Yang, Y. Fan, L. Mei, et al., "Synthesis of Atomically Thin Sheets by the Intercalation-Based Exfoliation of Layered Materials," *Nature Synthesis* 2 (2023): 101–118, https://doi.org/10.1038/s44160-022-00232-z.

11. Q. Zhang, L. Mei, X. Cao, Y. Tang, and Z. Zeng, "Intercalation and Exfoliation Chemistries of Transition Metal Dichalcogenides," *Journal of Materials Chemistry A* 8 (2020): 15417–15444, https://doi.org/10.1039/D0TA03727C.

12. B. Jennings and K. Parslow, "Particle-Size Measurement—The Equivalent Spherical Diameter," *Proceeding of the Royal Society A-Mathematical, Physical and Engineering Science* 419 (1988): 137–149, https://doi.org/10.1098/rspa.1988.0100.

13. D. Gantenbein, J. Schoelkopf, G. Matthews, and P. Gane, "Determining the Size Distribution-Defined Aspect Ratio of Platy Particles," *Applied Clay Science* 53 (2011): 544–552, https://doi.org/10.1016/j.clay.2011.04.020.

14. X. Tan, F. Liu, L. Hu, A. H. Reed, Y. Furukawa, and G. Zhang, "Evaluation of the Particle Sizes of Four Clay Minerals," *Applied Clay Science* 135 (2017): 313–324, https://doi.org/10.1016/j.clay.2016.10.012.

15. M. Nasser and A. James, "The Effect of Polyacrylamide Charge Density and Molecular Weight on the Flocculation and Sedimentation Behaviour of Kaolinite Suspensions," *Separation and Purification Technology* 52 (2006): 241–252, https://doi.org/10.1016/j.seppur.2006.04.005.

16. M. S. Arnold, A. A. Green, J. F. Hulvat, S. I. Stupp, and M. C. Hersam, "Sorting Carbon Nanotubes by Electronic Structure Using Density Differentiation," *Nature Nanotechnology* 1 (2006): 60–65, https://doi.org/10.1038/nnano.2006.52.

17. A. A. Green and M. C. Hersam, "Solution Phase Production of Graphene With Controlled Thickness via Density Differentiation," *Nano Letters* 9 (2009): 4031–4036, https://doi.org/10.1021/nl902200b.

18. J. Kang, J.-W. T. Seo, D. Alducin, A. Ponce, M. J. Yacaman, and M. C. Hersam, "Thickness Sorting of Two-dimensional Transition Metal Dichalcogenides via Copolymer-Assisted Density Gradient Ultracentrifugation," *Nature Communications* 5 (2014): 5478, https://doi.org/10.1038/ncomms6478.

19. X. Sun, D. Luo, J. Liu, and D. G. Evans, "Monodisperse Chemically Modified Graphene Obtained by Density Gradient Ultracentrifugal Rate Separation," *ACS Nano* 4 (2010): 3381–3389, https://doi.org/10.1021/nn1000386.

20. C. Backes, B. M. Szydlowska, A. Harvey, et al., "Production of Highly Monolayer Enriched Dispersions of Liquid-Exfoliated Nanosheets by Liquid Cascade Centrifugation," *ACS Nano* 10 (2016): 1589–1601, https://doi.org/10.1021/acsnano.5b07228.

21. K. Hantanasirisakul, T. Chantaurai, A. Limsukhon, P. Chomkhuntod, P. Poprom, and M. Sawangphruk, "Size Selection and Size-Dependent Optoelectronic and Electrochemical Properties of 2D Titanium Carbide (Ti 3 C 2 T x) MXene," *Advanced Materials Interfaces* 9 (2022): 2201457, https://doi.org/10.1002/admi.202201457.

22. C.-X. Hu, O. Read, Y. Shin, et al., "Effects of Lateral Size, Thickness, and Stabilizer Concentration on the Cytotoxicity of Defect-Free Graphene Nanosheets: Implications for Biological Applications," *ACS Applied Nano Materials* 5 (2022): 12626–12636, https://doi.org/10.1021/acsanm.2c02403.

23. S. Lindenthal, D. Fazzi, N. F. Zorn, et al., "Understanding the Optical Properties of Doped and Undoped 9-Armchair Graphene Nanoribbons in Dispersion," *ACS Nano* 17 (2023): 18240–18252, https://doi.org/10.1021/acsnano.3c05246.

24. S. Ott, N. Wolff, F. Rashvand, V. J. Rao, J. Zaumseil, and C. Backes, "Impact of the MoS_2Starting Material on the Dispersion Quality and Quantity After Liquid Phase Exfoliation," *Chemistry of Materials* 31 (2019): 8424–8431, https://doi.org/10.1021/acs.chemmater.9b02336.

25. V. J. Rao, H. Qi, F. J. Berger, et al., "Liquid Phase Exfoliation of Rubrene Single Crystals Into Nanorods and Nanobelts," *ACS Nano* 15 (2021): 20466–20477, https://doi.org/10.1021/acsnano.1c08965.

26. K. Synnatschke, S. Shao, J. van Dinter, et al., "Liquid Exfoliation of Ni 2 P 2 S 6: Structural Characterization, Size-Dependent Properties, and Degradation," *Chemistry of Materials* 31 (2019): 9127–9139, https://doi.org/10.1021/acs.chemmater.9b03468.

27. S. Xiang, P. Lu, Q. Zhang, et al., "Fluorographene With Narrow Lateral Size and Thickness Distributions Prepared for Enhancing Lubrication Performance of Bentonite Grease," *Journal of Wuhan University of Technology-Material Science Edition* 39 (2024): 1294–1302, https://doi.org/10.1007/s11595-024-2997-0.

28. R. Zribi, A. Foti, M. G. Donato, P. G. Gucciardi, and G. Neri, "Electrochemical and Sensing Properties of 2D-MoS_2 Nanosheets Produced via Liquid Cascade Centrifugation," *Electrochimica Acta* 436 (2022): 141433, https://doi.org/10.1016/j.electacta.2022.141433.

29. C. J. Zhang, S. Pinilla, N. McEvoy, et al., "Oxidation Stability of Colloidal Two-Dimensional Titanium Carbides (MXenes)," *Chemistry of Materials* 29 (2017): 4848–4856, https://doi.org/10.1021/acs.chemmater.7b00745.

30. T. Svedberg and J. Burton Nichols, "Determination of Size and Distribution of Size of Particle by Centrifugal Methods," *Journal of the American Chemical Society* 45 (1923): 2910–2917, https://doi.org/10.1021/ja01665a016.

31. F. I. Alzakia, W. Sun, S. J. Pennycook, and S. C. Tan, "Introducing Normalized Centrifugation for a More Accurate Thermodynamic Analysis of Molybdenum Disulfide Dispersions: A Study on Mixed Solvents of Alcohols and Amines with Water," *ACS Applied Materials & Interfaces* 12 (2020): 3096–3103, https://doi.org/10.1021/acsami.9b14510.

32. S. P. Ogilvie, M. J. Large, M. A. O'Mara, et al., "Size Selection of Liquid-Exfoliated 2D Nanosheets," *2D Materials* 6 (2019): 031002, https://doi.org/10.1088/2053-1583/ab0dc3.

33. M. S. Arnold, J. Suntivich, S. I. Stupp, and M. C. Hersam, "Hydrodynamic Characterization of Surfactant Encapsulated Carbon Nanotubes Using an Analytical Ultracentrifuge," *ACS Nano* 2 (2008): 2291–2300, https://doi.org/10.1021/nn800512t.

34. C. Backes, E. Karabudak, C. D. Schmidt, F. Hauke, A. Hirsch, and W. Wohlleben, "Determination of the Surfactant Density on SWCNTs by Analytical Ultracentrifugation," *Chemistry—A European Journal* 16 (2010): 13176–13184, https://doi.org/10.1002/chem.200903461.

35. J. Walter, T. J. Nacken, C. Damm, T. Thajudeen, S. Eigler, and W. Peukert, "Determination of the Lateral Dimension of Graphene Oxide Nanosheets Using Analytical Ultracentrifugation," *Small* 11 (2015): 814–825, https://doi.org/10.1002/smll.201401940.

36. C. Damm, D. Long, J. Walter, and W. Peukert, "Size and Shape Selective Classification of Nanoparticles," *Powders* 3 (2024): 255–279.

37. P. Atkins and J. de Paula, Atkins' Physical Chemistry, in *Macromolecules and Self-Assembly* (Oxford University Press, 2014), 726–728.

38. K. E. van Holde, W. C. Johnson, and P. S. Ho, *Principles of physical biochemistry*, 2nd. ed., Pearson Education International, Upper Saddle River N. J (2006).

39. F. Perrin, "Mouvement Brownien d'un Ellipsoide—I. Dispersion Diélectrique pour Des Molécules Ellipsoidales," *Journal De Physique Et Le Radium* 5 (1934): 497–511, https://doi.org/10.1051/jphysrad:01934005010049700.

40. R. Gopalakrishnan, T. Thajudeen, and C. J. Hogan, "Collision Limited Reaction Rates for Arbitrarily Shaped Particles Across the Entire Diffusive Knudsen Number Range," *Journal of Chemical Physics* 135 (2011): 054302, https://doi.org/10.1063/1.3617251.

41. F. van der Kooij, A. Philipse, and J. Dhont, "Sedimentation and Diffusion in Suspensions of Sterically Stabilized Colloidal Platelets," *Langmuir* 16 (2000): 5317–5323, https://doi.org/10.1021/la991571b.

42. J. Vinograd, R. Bruner, R. Kent, and J. Weigle, "Band-Centrifugation of Macromolecules and Viruses in Self-Generating Density Gradients," *Proceedings of the National Academy of Sciences* 49 (1963): 902–910, https://doi.org/10.1073/pnas.49.6.902.

43. J. Vinograd and R. Bruner, "Band Centrifugation of Macromolecules in Self-Generating Density Gradients. III. Conditions for Convection-Free Band Sedimentation," *Biopolymers* 4 (1966): 157–170, https://doi.org/10.1002/bip.1966.360040203.

44. J. Vinograd and R. Bruner, "Band Centrifugation of Macromolecules in Self-Generating Density Gradients. II. Sedimentation and Diffusion of Macromolecules in Bands," *Biopolymers* 4 (1966): 131–156, https://doi.org/10.1002/bip.1966.360040202.

45. H. Li, L. Beetsma, S. Prakash, M. Mikkers, and L. Botto, "Analysis and Optimization of a Multicascade Method for the Size Fractionation of Poly-Dispersed Particle Systems Via Sedimentation or Centrifugation," arXiv preprint arXiv:2303.05257 (2023).

46. C. M. Schneider and H. Cölfen, "Analytical Band Centrifugation Revisited," *European Biophysics Journal* 47 (2018): 799–807, https://doi.org/10.1007/s00249-018-1315-1.

47. N. Kubetschek, C. Backes, and S. Goldie, "Algorithm for Reproducible Analysis of Semiconducting 2D Nanomaterials Based on UV-VIS Spectroscopy," *Advanced Materials Interfaces* 11 (2024): 2400311, https://doi.org/10.1002/admi.202400311.

48. C. Backes, K. R. Paton, D. Hanlon, et al., "Spectroscopic Metrics Allow In Situ Measurement of Mean Size and Thickness of Liquid-Exfoliated Few-Layer Graphene Nanosheets," *Nanoscale* 8 (2016): 4311–4323, https://doi.org/10.1039/C5NR08047A.

49. C. Gabbett, A. G. Kelly, E. Coleman, et al., "Understanding How Junction Resistances Impact the Conduction Mechanism in Nano-Networks," *Nature Communications* 15 (2024): 4517, https://doi.org/10.1038/s41467-024-48614-5.

50. C. Backes, D. Campi, B. M. Szydlowska, et al., "Equipartition of Energy Defines the Size–Thickness Relationship in Liquid-Exfoliated Nanosheets," *ACS Nano* 13 (2019): 7050–7061, https://doi.org/10.1021/acsnano.9b02234.

51. J. Kestin, N. Imaishi, S. H. Nott, J. C. Nieuwoudt, and J. V. Sengers, "Viscosity of Light and Heavy Water and Their Mixtures," *Physica A: Statistical Mechanics and Its Applications* 134 (1985): 38–58, https://doi.org/10.1016/0378-4371(85)90155-4.

52. A. E. Boycott, "Sedimentation of Blood Corpuscles," *Nature* 104 (1920): 532–532, https://doi.org/10.1038/104532b0.

53. W. D. Hill, R. R. Rothfus, and K. Li, "Boundary-enhanced Sedimentation Due to Settling Convection," *International Journal of Multiphase Flow* 3 (1977): 561–583, https://doi.org/10.1016/0301-9322(77)90030-1.

54. E. Ponder, "On Sedimentation and Rouleaux Formation—II," *Quarterly Journal of Experimental Physiology* 16 (1926): 173–194, https://doi.org/10.1113/expphysiol.1926.sp000380.

55. M.-J. Lee, Y.-J. Chang, C.-J. Cheng, Y.-C. Yeh, C.-F. Chen, and Y.-J. Chou, "A Theoretical Framework to Determine the Optimal Centrifugation Angle for Separation of Plasma From Blood Samples," *Sensors and Actuators A: Physical* 353 (2023): 114234, https://doi.org/10.1016/j.sna.2023.114234.

56. T. F. D. Fernandes, D. R. Miquita, E. M. Soares, A. P. Santos, L. G. Cançado, and B. R. A. Neves, "A Semi-automated General Statistical Treatment of Graphene Systems," *2D Materials* 7 (2020): 025045, https://doi.org/10.1088/2053-1583/ab7975.

57. J. C. C. Santos, M. C. Prado, H. L. O. Morais, et al., "Topological Vectors as a Fingerprinting System for 2D-Material Flake Distributions," *NPJ 2D Materials and Applications* 5 (2021): 51, https://doi.org/10.1038/s41699-021-00234-z.

58. H. Chacham, J. C. C. Santos, F. G. Pacheco, et al., "Controlling the Morphology of Nanoflakes Obtained by Liquid-Phase Exfoliation: Implications for the Mass Production of 2D Materials," *ACS Applied Nano Materials* 3 (2020): 12095–12105, https://doi.org/10.1021/acsanm.0c02598.

59. K. Synnatschke, P. A. Cieslik, A. Harvey, et al., "Length- and Thickness-Dependent Optical Response of Liquid-Exfoliated Transition Metal Dichalcogenides," *Chemistry of Materials* 31 (2019): 10049–10062, https://doi.org/10.1021/acs.chemmater.9b02905.

60. K. Synnatschke, N. Moses Badlyan, A. Wrzesinska, et al., "Sonication-assisted Liquid Phase Exfoliation of Two-Dimensional $CrTe_3$ Under Inert Conditions," *Ultrasonics Sonochemistry* 98 (2023): 106528, https://doi.org/10.1016/j.ultsonch.2023.106528.

61. K. Synnatschke, J. van Dinter, A. Müller, et al., "Exfoliablity, Magnetism, Energy Storage and Stability of Metal Thiophosphate Nanosheets Made in Liquid Medium," *2D Materials* 10 (2023): 024003, https://doi.org/10.1088/2053-1583/acba2c.

62. A. Griffin, A. Harvey, B. Cunningham, et al., "Spectroscopic Size and Thickness Metrics for Liquid-Exfoliated h-BN," *Chemistry of Materials* 30 (2018): 1998–2005, https://doi.org/10.1021/acs.chemmater.7b05188.

63. A. Harvey, C. Backes, J. B. Boland, et al., "Non-Resonant Light Scattering in Dispersions of 2D Nanosheets," *Nature Communications* 9 (2018): 4553, https://doi.org/10.1038/s41467-018-07005-3.

64. L. Ueberricke, J. N. Coleman, and C. Backes, "Robustness of Size Selection and Spectroscopic Size, Thickness and Monolayer Metrics of Liquid-Exfoliated WS 2," *Physica Status Solidi (b)* 254 (2017): 1700443, https://doi.org/10.1002/pssb.201700443.

Supporting Information

Additional supporting information can be found online in the Supporting Information section.

Supporting file 1: admi70310-sup-0002-DataFile.xlsx **Supporting file 2**: admi70310-sup-0002-DataFile.xlsx